Atmos. Chem. Phys., 26, 2785–2796, 2026
https://doi.org/10.5194/acp-26-2785-2026

Atmospheric Chemistry and Physics
Open Access
EGU

Understanding divergent brown carbon photobleaching rates from molecular perspective

Yanting Qiu[1], Tao Qiu[2], Yuechen Liu[3], Yu Gu[2], Ruiqi Man[1], Dapeng Liang[2], Taomou Zong[1], Zhijun Wu[1,4], and Min Hu[1,4]

[1]State Key Laboratory of Regional Environment and Sustainability, International Joint Research Center for Atmospheric Research (IJRC), College of Environmental Sciences and Engineering, Peking University, Beijing, 100871, China
[2]Key Lab of Groundwater Resources and Environment of the Ministry of Education, College of New Energy and Environment, Jilin University, Changchun 130012, China
[3]National Institute of Metrology, Beijing 100029, China
[4]Collaborative Innovation Center of Atmospheric Environment and Equipment Technology, Nanjing University of Information Science and Technology, 210044, Nanjing, China

Correspondence: Zhijun Wu (zhijunwu@pku.edu.cn)

Received: 6 November 2025 – Discussion started: 20 November 2025
Revised: 4 February 2026 – Accepted: 10 February 2026 – Published: 24 February 2026

Abstract. The global radiative effect of brown carbon (BrC) remains highly uncertain. BrC's photobleaching, which significantly affects its radiative effect, has been still poorly constrained. This study investigates and compares photobleaching rates of laboratory-synthesized secondary BrC (aq-BrC), biomass burning-derived BrC (b-BrC), and ambient $PM_{2.5}$-derived BrC (p-BrC) to illustrate the variability in BrC photobleaching kinetics from different types of BrC reported in prior studies. Our results reveal a source dependence in BrC photobleaching rates. The highest photobleaching rate constant (k_{BrC}) is observed for aq-BrC ($1.13 \pm 0.08\,h^{-1}$), followed by p-BrC ($0.12 \pm 0.02\,h^{-1}$) and b-BrC ($0.05 \pm 0.01\,h^{-1}$), indicating the stable light-absorption capacity of b-BrC in the atmosphere. Integration of these rate constants with data derived from previous studies highlighted the differences in photobleaching behaviors among BrC from different sources. The OH oxidation of imidazole-2-carboxaldehyde (2-IC) and methylglyoxal oligomers, nitrophenols (including phenols), and lignin derivatives governs the photobleaching of aq-BrC, p-BrC, and b-BrC, respectively. The high k_{BrC} of aq-BrC is attributed to the high reactivity of the chain structures in 2-IC and methylglyoxal oligomers. In contrast, the highly conjugated structures of lignin derivatives in b-BrC impart stability against OH oxidation, resulting in a low k_{BrC}. Our findings reveal the significant differences in the photobleaching behavior of BrC originated from different sources, underscoring the crucial need to account for source differences in assessments of BrC's global radiative forcing effect.

1 Introduction

Brown carbon (BrC) is a significant contributor to atmospheric warming (Saleh, 2020; Chung et al., 2012; Brown et al., 2021) and Earth's radiative budget (Bond, 2001; Kirchstetter et al., 2004; Wang et al., 2018, 2022) due to its ultraviolet-visible (UV-Vis) light absorption. The BrC's direct radiative effect (DRE), accounting for 20 %–40 % of total DRE caused by light-absorbing carbonaceous aerosols (Heald et al., 2014; Jo et al., 2016; Saleh et al., 2015; Wang et al., 2018, 2014), remains highly uncertainty. BrC with global average DRE values varying from +0.03 to +0.57 $W\,m^{-2}$ is considered as the least understood warming agents in the atmosphere (Zhang et al., 2020; Zeng et al., 2020; Corr et al., 2012).

BrC comprises abundant chemically reactive species that react readily with atmospheric reactive gases and radicals

(Aiona et al., 2017; Fleming et al., 2020; Hems et al., 2021; Liu et al., 2020), modifying its light-absorption properties. Both laboratory experiments (Borduas-Dedekind et al., 2019; Fleming et al., 2019; Hems and Abbatt, 2018; Hems et al., 2020; Schnitzler and Abbatt, 2018; Schnitzler et al., 2022) and field campaigns (Dasari et al., 2019; Qiu et al., 2024; Wang et al., 2014; Xu et al., 2024; Zeng et al., 2020) consistently found that BrC's photochemical aging process reduced its mass absorption coefficient (MAC), which is also known as photobleaching. In current models, the evaluation of BrC photobleaching on its radiative forcing effect mainly depends on the temporal decline in BrC's light-absorption capacity (Schnitzler et al., 2022; Wang et al., 2018; Xu et al., 2024), i.e., the photobleaching rate, which is substantial variability across different laboratory experiments and field observations. Notably, BrC generated from aqueous-phase reactions often exhibits negligible absorbance in the UV-Vis range after less than 2 h of radiation (Aiona et al., 2017). Field observations reveal that atmospheric BrC undergoes a MAC reduction exceeding 60 % after 1 d of sunlight exposure (Müller et al., 2023; Qiu et al., 2024). In comparison, over the same 1 d of solar radiation, the reduction in the MAC of BrC derived from biomass burning is much lower than atmospheric BrC (Fan et al., 2019; Fleming et al., 2020; Müller et al., 2023; Wong et al., 2019). Accurately determining BrC's photobleaching rate is paramount for quantifying the impact of BrC photobleaching on its radiative forcing effect in models.

Furthermore, BrC's chemical composition fundamentally governs its photochemical reactivity (Hems et al., 2021; Hems and Abbatt, 2018; Dalton and Nizkorodov, 2021; Liu et al., 2025), thereby modulating its photobleaching rate. However, the relationship between changes in BrC's molecular composition and light absorption properties during photobleaching is still poorly constrained. This knowledge gap leads to significant uncertainty in evaluating the evolution of BrC's light absorption capacity during atmospheric transportation. For instance, BrC emitted from biomass burning has been observed to retain strong absorption after several days of transport to the Arctic region (Yue et al., 2022). In contrast, model simulations estimate BrC is nearly complete photobleaching over this timescale (Wang et al., 2018; Xu et al., 2024), which contradicts the observational evidence. Elucidating the linkage between BrC molecular composition and photobleaching rates would improve the accuracy of global-scale assessments of BrC's dynamic light absorption properties during long-range transport.

In this work, we performed photochemical aging experiments on three types of BrC under identical, controlled conditions, including synthesized by aqueous phase reaction (referred to "aq-BrC"), and extracted from ambient (referred to "p-BrC", where "p" denotes particulate) and biomass burning (referred to "b-BrC") $PM_{2.5}$ samples. Compared to previous studies, this work systematically investigated the differences in photobleaching kinetics among various types of BrC under identical environmental conditions. We combine this with high-resolution mass spectrometry (HRMS) analysis to establish a mechanistic link between the observed divergent BrC photobleaching rates and the evolution of key chromophores. In addition, we quantify the contribution of the OH oxidation pathway across all BrC types. These findings aim to provide essential parameters and a mechanistic basis for improving the representation of BrC photochemical aging in climate models.

2 Methodology

2.1 Preparation of BrC

Methylglyoxal (MG, 40 wt %, Merck) and ammonium sulfate (AS, 98 %, Alaadin) solutions (1 mol L^{-1}) was mixed in darkness at room temperature for 24 h (pH 3.7–4.2) (Yang et al., 2024) to generate aq-BrC. Residual MG/AS were removed by solid-phase extraction (SPE) (Lin et al., 2010; Wang et al., 2017). The eluent was dried under gentle stream of ultrapure N_2 (> 99.99 %) and reconstituted in ultrapure water (18.2 MΩ cm). Previous studies have confirmed that MG is one of the most abundant dicarbonyl species in the atmosphere (Gu et al., 2025; Fu et al., 2008), which is produced by primary emissions and oxidation of volatile organic compounds (VOCs). Considering that MG exhibit a tendency to partition into aqueous aerosols and cloud droplets in the atmosphere (Laskin et al., 2015), therefore, the secondary BrC generated by the aqueous-phase reaction between MG and AS is representative as aq-BrC.

$PM_{2.5}$ samples emitted from corn straw combustion in household stoves was collected on quartz fiber filters (25 × 20 cm, Whatman) using a high-volume sampler (TH-1000H, Wuhan Tianhong; 1.05 m^3 min^{-1}). Corn straw is recognized as a typical and common domestic biomass fuel in China, constituting approximately 40.0 % of the total output from the agricultural products and has an estimated annual production of about 295 × 10^6 t. Therefore, $PM_{2.5}$ emitted from corn straw combustion was selected as typical biomass burning aerosols in this work. Figure S1 in the Supplement shows a schematic of sample collection process of biomass burning $PM_{2.5}$ samples, and Table S1 summarizes the concentrations of organic carbon (OC), element carbon (EC), the concentration of total organic carbon (TOC) of each sample. This approach closely represents real-world biomass burning emissions (Chen et al., 2019; Shan et al., 2017). For each sample, background aerosols were collected for 1 h both before to and after the sampling period.

We selected five atmospheric $PM_{2.5}$ samples collected at Peking University Changping Campus (40°8′ N, 116°6′ E) from 15 December 2020 to 15 January 2021 to extract p-BrC. Table S2 summarizes the sampling time and average $PM_{2.5}$ mass concentrations during sampling of each sample. All samples were collected using a high-volume sampler with the flow rate of 1.05 m^3 min^{-1}. Gaseous pollutants,

$PM_{2.5}$ mass concentrations, non-refractory submicron particles (NR-PM_1) chemical composition, and meteorology parameters were monitored (Fig. S2; details in Table S3).

For those $PM_{2.5}$ samples, twenty 1.5-cm^2 filter sections were ultrasonically extracted in LC-MS grade methanol (Merck Inc.) for twice (20 min) to extract p-BrC and b-BrC. Extracts were dried gentle stream of ultrapure N_2 (> 99.99 %) and redissolved in ultrapure water.

2.2 Laboratory aqueous-phase photochemical aging setup

Photochemical aging experiments were conducted in a temperature-controlled ($20 \pm 0.1°$) chamber, equipped with 20 UV bulbs (40 W; $\lambda_{max} = 370$ nm). The TOC of all BrC solutions were adjusted to 50 mgC L^{-1}. BrC solutions were irradiated in quartz bottles (10 mL) with added H_2O_2 (30 wt %, Alaadin) to generate OH radicals. Steady-state OH concentrations ($[OH]_{ss}$) were quantified via pseudo-first-order decay of benzoic acid (methods detailed in Sect. S1) (Hems and Abbatt, 2018). The average $[OH]_{ss}$ was $(3.17 \pm 0.47) \times 10^{-14}$ mol L^{-1}, slightly below typical cloud water maxima.

The transition from laboratory experimental illumination to actual solar radiation was applied by calculating the ratio between laboratory and actual spectral flux densities following the identical calculation approach used in our previous study (Qiu et al., 2024). Briefly, the scaling factor can be approximated as the ratio between the integrated spectral flux densities of two different light sources. The spectral flux densities of the UV bulbs used in this work and the 24-hour average Beijing solar spectrum at 300 m above sea level were integrated from 360 to 380 nm (see Sect. S2 for detail). The 24-hour average Beijing solar spectrum was simulated using the Tropospheric Ultraviolet and Visible Radiation model (Table S4), and Fig. S3 shows the comparison between calculated and measured radiation spectrum. The calculated scaling factor in this work is 3.86 (Qiu et al., 2024). Samples were collected at 0, 2, 4, 8, and 16 h of equivalent solar radiation.

Furthermore, a series of control experiments were performed under H_2O_2 free and dark conditions. The former consisted of 16 h of radiation in the absence of H_2O_2. The dark experiments involved storing the solutions in complete darkness for an identical period (16 h) to account for any non-photochemical changes.

These experiments were configured to delineate the contributions of different pathways to BrC photobleaching. The H_2O_2 added photochemical aging experiments elucidates the synergistic effect of OH oxidation, direct BrC photolysis, and other light-independent reactions occur in dark conditions. The H_2O_2 free experiments considered the sole contribution of the direct photolytic pathway. In addition, the dark control experiments served to investigate any potential influence of chemical reactions in dark conditions on the BrC's light-absorption capacity.

2.3 Light-absorption properties and molecular composition analysis of BrC

UV-Vis absorption spectra (250–700 nm) were recorded using a spectrophotometer (UV-1780, Shimadzu Inc.). MAC normalized absorption to TOC concentrations. In Eq. (1), $A_{10}^{abs}(\lambda)$, b, and c denotes the measured base-10 absorbance, optical path length (1 cm), and measured TOC, respectively.

$$\mathrm{MAC}(\lambda) = \frac{A_{10}^{abs}(\lambda) \times \ln(10)}{b \times c} \quad (1)$$

BrC's molecular composition was analyzed via HRMS (Orbitrap Fusion™ Tribrid™, Thermo Scientific) with electrospray ionization (ESI) in negative mode (ESI(-); m/z 70–700). Samples were directly injected into HRMS at a flow rate of 10 µL min^{-1}. Triplicate analyses ensured reproducibility, with only peaks detected in all replicates retained for assignment. Molecular formulas ($C_xH_yO_zN_wS_n$; x = 1–90, y = 1–200, z = 0–20, w = 0–3, n = 0–1) were assigned with m/z error lower than ± 0.005 Da. The H/C, O/C, N/C, and S/C atom ratios for each assigned formula were constrained to 0.3–3.0, 0–3.0, 0–0.5, and 0–2.0, respectively (Wang et al., 2017). Signal-intensity-weighted average elemental compositions (Eq. 2), O/C atom ratios, and N/C atom ratios (Eq. 3) were calculated as:

$$Y = \frac{\sum_i x_i Y_i}{\sum_i x_i}, \text{ where } Y = \mathrm{C, H, O, N, and S} \quad (2)$$

$$Y/Z = \frac{\sum_i x_i Y_i}{\sum_i x_i Z_i}, \text{ where } Y/Z = \mathrm{O/C \text{ or } N/C} \quad (3)$$

where x_i in Eqs. (2) and (3) indicated the signal-intensity-weighted factor.

3 Results and Discussion

3.1 Quantification and Comparison of BrC Photobleaching Rates

Given that BrC's light-absorption properties at shorter wavelengths are a better indicator of its photobleaching kinetics (Aiona et al., 2017), we focused our analysis on the variation in the MAC at 300 nm (MAC_{300}). The measured MAC_{300} of aq-BrC, p-BrC, and b-BrC is $(7.32 \pm 0.89) \times 10^3$ cm^2 g^{-1}, $(7.38 \pm 0.83) \times 10^2$ cm^2 g^{-1}, and $(9.44 \pm 0.71) \times 10^3$ cm^2 g^{-1}, respectively. Figure 1a shows the overall decay of MAC_{300} for different BrC types, plotted as the natural logarithm of the ratio ($\ln(MAC_{300,t}/MAC_{300,0})$) versus irradiation hours. The left axis of Fig. 1a shows the variation in $\ln(MAC_{300,t}/MAC_{300,0})$ for p-BrC and b-BrC, while the right axis denotes this variation for aq-BrC. Here, $MAC_{300,t}$

and $MAC_{300,0}$ denote the MAC_{300} after t hours of irradiation and its initial value, respectively. The observed linear decay demonstrates that BrC undergoes photobleaching regardless of its source. The aq-BrC has been almost completely bleached in the initial 2 h. For p-BrC, the MAC_{300} decreased by 77.2 % after 16 h of radiation. In comparison, for b-BrC, the MAC_{300} only decreased by 56.1 %. Even after extending to 32 h of radiation, b-BrC still kept strong light-absorption capacity (see Fig. S4). The differences in the variation in MAC_{300} for different types of BrC demonstrate that aq-BrC undergoes rapid photobleaching in the presence of solar radiation, while b-BrC exhibits stable light-absorption capacity during photobleaching.

The liner decline in $\ln(MAC_{300,t}/MAC_{300,0})$ indicates that BrC photobleaching fitted the pseudo-first order kinetic, which was represented by the negative slope of $\ln(MAC_{300,t}/MAC_{300,0})$ vs. radiation hours:

$$MAC_{300,t} = MAC_{300,0} \times \exp(-k_{BrC}t) \quad (4)$$

where k_{BrC} is the overall photobleaching rate constant. The calculated k_{BrC} of aq-BrC, p-BrC, and b-BrC were (1.13 ± 0.08), (0.12 ± 0.02), and $(0.05 \pm 0.01)\,h^{-1}$, respectively. Correspondingly, the lifetime of BrC (τ_{BrC}, indicated by BrC's absorption decreased to $1/e$ of its initial value) (Schnitzler et al., 2022) were 1.05, 10.91, and 19.16 h, respectively. Longer τ_{BrC} of b-BrC indicates its absorption largely retains during atmospheric transportation process. This order-of-magnitude difference in k_{BrC} among three BrC types, quantified under comparable conditions, highlights a fundamental source dependency that cannot be attributed to environmental condition variability. This clear difference necessitates a molecular-level explanation, which we pursue by examining the dominant photobleaching pathway and the underlying chemical composition.

Figure 1b presents a comparison of MAC_{300} versus overall k_{BrC} for BrC from various sources, including data from this study and other studies (data and references in Table S5). Based on their sources, we classified aq-BrC (including BrC generated via aldehyde-amine condensation reactions), p-BrC, and b-BrC (including representative compounds emitted from biomass burning) in three different clusters. Our results are comparable to those of previous studies. The characteristic of aq-BrC is strong absorption, rapid photobleaching. This demonstrates that the light-absorption capacity of BrC generated by secondary atmospheric aqueous phase reactions (De Haan et al., 2017) decrease rapidly in the presence of solar radiation. In stark contrast, b-BrC shows strong absorption but slow photobleaching, implying its stable strong absorption in the atmosphere. p-BrC exhibits weak absorption and slow photobleaching, which has also been observed in different urban areas, including Eastern China (Qiu et al., 2024), India (Dasari et al., 2019), Northern Europe (Müller et al., 2023), and the United States (Chen et al., 2021). It is noteworthy that p-BrC contains a mixture of primary and secondary BrC that is challenging to separate quantitatively. However, from molecular composition and solar radiation during sampling, p-BrC is considered to be predominantly of primary emissions. Herein, we further analyzed the molecular composition of p-BrC following the non-target analysis approach used in our previous study (Qiu et al., 2024), more details were described in Sect. S3. Figure S5 shows the molecular composition and relevant solar radiation during sampling, which is represented by the 75th percentile solar radiation (Rad_{75}). Low Rad_{75} showed limited photochemical aging prior to analysis, and high mass fraction of nitrophenols proved the dominate role of primary emission for p-BrC.

Having investigated the differences in overall photobleaching rates across different BrC types, we further elucidated the underlying mechanisms by assessing the contribution of each photobleaching pathway. Previous studies suggest that BrC photobleaching occurs via three different pathways, including direct photolysis, OH oxidation, and other light-independent reactions occur in dark conditions (Gao and Zhang, 2019; Liu-Kang et al., 2022; Wong et al., 2019). Choudhary et al. (2023) have demonstrated that in the presence of H_2O_2, the overall k_{BrC} can be expressed as a linear sum of the pseudo first-order effective photobleaching rate constant due to OH oxidation ($k_{BrC,OH}$), BrC direct photolysis ($k_{BrC,pho}$), and other light-independent reactions occur in dark conditions ($k_{BrC,ctrl}$), see Eq. (3):

$$k_{BrC} = k_{BrC,OH} + k_{BrC,pho} + k_{BrC,ctrl} \quad (5)$$

The $k_{BrC,pho}$ and $k_{BrC,ctrl}$ are derived from the pseudo-first-order decay of MAC_{300} in H_2O_2 free experiments and dark control experiments, respectively, using the calculation approach identical to Eq. (2) and the experimental procedures detailed in Sect. 2.2. Therefore, although $k_{BrC,OH}$ cannot be measured directly, it can be indirectly determined by calculating the difference between the overall k_{BrC} and the sum of $k_{BrC,pho}$ (from H_2O_2 free experiments) and $k_{BrC,ctrl}$ (from dark control experiments).

Figure 2 displays the variations in MAC_{300} in photochemical aging experiments (with H_2O_2, red line, representing the synergistic effect of OH oxidation, direct BrC photolysis, and other light-independent reactions occur in dark conditions), H_2O_2 free experiments (blue line, representing the contribution of BrC direct photolysis), and dark control experiments (black line, representing the contribution of other light-independent reactions occur in dark conditions). It is noted that for dark control experiments, the x-axis denotes the time the BrC solution is kept under dark conditions. Table 1 summarizes the $k_{BrC,ctrl}$, $k_{BrC,pho}$, and $k_{BrC,OH}$ for different BrC types. Specifically, MAC_{300} variations were negligible in dark controls, rendering the calculated $k_{BrC,ctrl}$ was close to 0. For all BrC types, $k_{BrC,pho}$ was substantially lower than $k_{BrC,OH}$. The overwhelming contribution of $k_{BrC,OH}$ (over 80 % of k_{BrC}) unambiguously identifies OH oxidation as the dominant mechanism governing BrC photobleaching. The dominate role of OH oxidation in BrC photobleaching

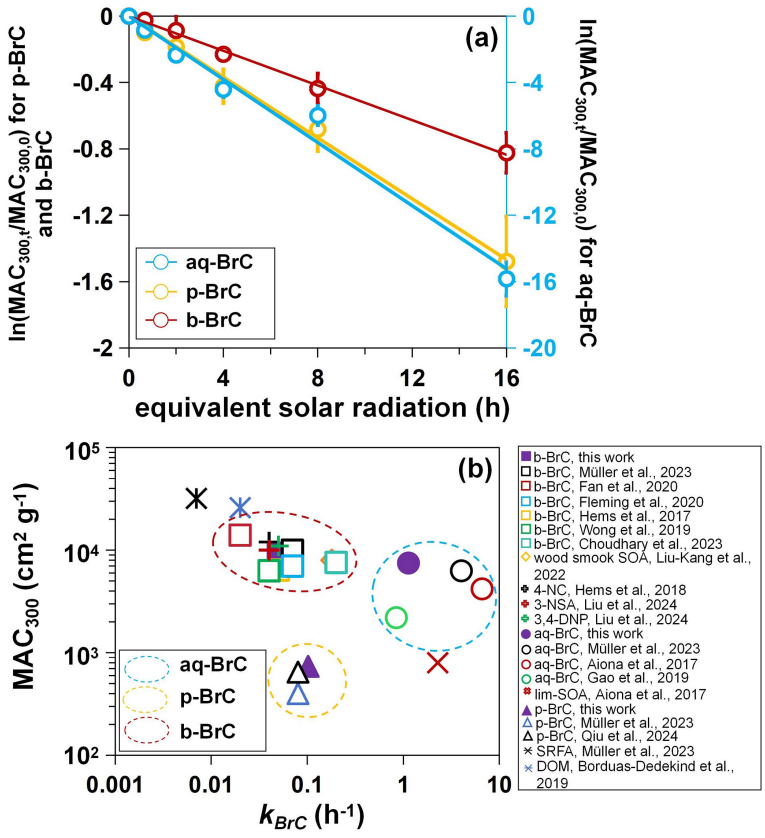

Figure 1. **(a)** Variations in the $\ln(MAC_{300,t}/MAC_{300,0})$ of aq-BrC (blue plots, right axis), p-BrC (yellow plots, left axis), and b-BrC (red plots, left axis) as a function of radiation hours. Blue, yellow, and red lines indicate fitted k_{BrC} of aq-BrC, p-BrC, and b-BrC. Error bars represent one standard deviation of datapoints derive from three (aq-BrC and b-BrC) or five (p-BrC) parallel experiments. **(b)** The relationship between MAC_{300} and calculated k_{BrC} of different types of BrC in this work and other studies. 4-NC, 3-NSA, 3,4-DNP, SRFA, and DOM represents 4-nitrocateol, 3-mitrosalicylic acid, 3,4-dinitrophenol, Suwannee River fulvic acid standard, and dissolved organic matters, respectively. Blue, yellow, and red circles marked aq-BrC (including BrC generated via aldehyde-amine condensation reactions), p-BrC, and b-BrC (including representative compounds emitted from biomass burning). The exact MAC_{300} values are obtained from figures in corresponding literatures, and k_{BrC} are calculated based on the MAC_{300} and hours of radiation.

Table 1. The $k_{BrC,ctrl}$, $k_{BrC,pho}$, and $k_{BrC,OH}$ for different BrC types.

BrC type	$k_{BrC,ctrl}$	$k_{BrC,pho}$	$k_{BrC,OH}$
aq-BrC	$(0.004 \pm 0.002)\,h^{-1}$	$(0.19 \pm 0.03)\,h^{-1}$	$(0.94 \pm 0.06)\,h^{-1}$
p-BrC	$(0.007 \pm 0.001)\,h^{-1}$	$(0.02 \pm 0.005)\,h^{-1}$	$(0.08 \pm 0.02)\,h^{-1}$
b-BrC	$(0.006 \pm 0.002)\,h^{-1}$	$(0.01 \pm 0.004)\,h^{-1}$	$(0.04 \pm 0.01)\,h^{-1}$

have been also proved in several previous studies (Choudhary et al., 2023; Hems and Abbatt, 2018; Zhao et al., 2015), this work provide quantitative and comparative evidence regardless of BrC types. Consequently, the observed differences in k_{BrC} among different types of BrC can be fundamentally attributed to the molecular-composition-dependent reactivity of BrC components toward OH radicals. Hence, understanding the underlying molecular composition that determine a BrC molecule's susceptibility to this OH oxidation.

It is important to note that the laboratory-synthesized aq-BrC represents a simplified chemical system. While it provides a clear mechanistic understanding of rapid photobleaching driven by BrC chromophores with high chemical reactivity, real atmospheric aqueous-phase processes involve more complex precursors and mixtures, yielding secondary BrC with different photobleaching kinetics. Nevertheless, the dominate role of OH oxidation established in this work, which provides a critical lens through which to inter-

pret the slower photobleaching rates of the more complex ambient (p-BrC) and biomass burning (b-BrC) samples.

3.2 Chemical investigation of different BrC photobleaching rates

To elucidating the differences in BrC photobleaching rates, we investigated BrC's molecular composition before and after photobleaching, which was represented by BrC's molecular composition after 16 h of radiation.

Table 2 summarizes the signal-intensity-weighted average elemental compositions, molecular weights, O/C ratios, and N/C ratios of different types of BrC before and after 16 h of radiation. The observed decrease in average molecular weights upon photobleaching across all BrC types, alongside an elevated O/C ratio, points to the production of more oxidized, lower-mass species. Additionally, we found the mass concentrations of low-molecular-weight organic acids (formic acid, acetic acid, and oxalic acid; see Fig. S6) significantly increased with longer radiation hours, demonstrating carbon backbone fragmentation (Borduas-Dedekind et al., 2019). Figure S7 demonstrates that more products with lower C atom numbers are detected after photobleaching, further proves the carbon backbone fragmentation. Considering OH oxidation dominates BrC photobleaching, the molecular-level evolution aligns with OH-mediated degradation pathways (Hems et al., 2020; Qiu et al., 2024; Liu et al., 2025): (i) electrophilic addition to unsaturated bonds (like C = C bonds) and (ii) subsequent carbon backbone fragmentation.

In addition, the reduced N/C atom ratios (Table 2) further confirmed degradation of N-containing compounds, which are key UV-Vis absorbers contributing significantly to BrC absorption (Lin et al., 2017; Wang et al., 2019; Zeng et al., 2021; Li et al., 2025). The formation of compounds with higher oxidation states and the degradation of N-containing compounds reduce the conjunction degrees of BrC, diminishing $\pi \rightarrow \pi*$ electronic transitions and weakening light-absorption capacity.

Subsequently, we determined representative BrC chromophores relate to the photobleaching of different types of BrC based on the following three criteria. Firstly, we calculated the differential HRMS spectra of different types of BrC before and after photobleaching (Fig. S8). These peaks with negative intensities (> 3 times the signal-to-noise ratio) denote species consumed after photobleaching. Secondly, these candidate species were cross-compared to identify compounds that were highly characteristic of each specific source. Lastly, tandem HRMS ($HRMS^2$) analysis was adopted to determine the chemical structure of selected BrC chromophores.

In this work, the photooxidation of MG and imidazole-2-carboxaldehyde (2-IC) oligomers (Aiona et al., 2017) with formula $C_{3n}H_{4n}N_2O_{2n-3}$ ($n = 2$–5; including m/z 123.06, 195.08, 267.10, and 339.12), phenols and nitrophenols (Hems and Abbatt, 2018; Magalhães et al., 2017) (including m/z 109.03, 138.02, 152.03, 168.03, 182.01, and 183.00), and lignin derivatives (Fleming et al., 2020) (including m/z 137.02, 163.04, 245.08, 283.06, and 313.07) were identified as the dominant reactions in the photobleaching of aq-BrC, p-BrC, and b-BrC, respectively. Compounds identified as products after photobleaching for aq-BrC, p-BrC, and b-BrC are respectively summarized in Tables S6–S8. It is acknowledged that secondary BrC comprises a wide variety of compounds formed through different pathways. While phenols and nitrophenols identified here can themselves be secondary products, their markedly slower photobleaching rate (compared to the MG/AS-derived aq-BrC in this work) highlights the substantial kinetic diversity within the broader secondary BrC. This further reinforces that the molecular architecture, rather than the primary or secondary classification, is the fundamental determinant of BrC photochemical stability.

Figure 3 displays the chemical structures of these MG and 2-IC oligomers, phenols and nitrophenols, and lignin derivatives, as well as the declines in their signal intensities after 16 h of radiation. Variations in HRMS signal intensities represent the changes in the mass concentrations, though specific mass concentrations cannot be derived. Figure 3a illustrates the predominant molecular species and the corresponding decline in MG and 2-IC oligomers during the photobleaching of aq-BrC. Following photobleaching, these oligomers became undetectable (signal-to-noise ratio < 3), experiencing a reduction in signal intensity of $> 99.9\,\%$ (Fig. 3a). This observation is consistent with the nearly complete bleaching of aq-BrC. The high reactivity of the chain structures of MG and 2-IC oligomers with OH radicals (Aiona et al., 2017) explains the elevated k_{BrC} value observed for aq-BrC.

As shown in Fig. 3b, a greater number of electron-withdrawing substituents on the benzene ring correlates with a more significant decline of signal intensity after photobleaching. For instance, 2-methyl-4-nitrophenol (m/z 152.03), which bears an electron-donating methyl group in addition to the electron-withdrawing nitro substituent present in 4-nitrophenol (m/z 138.02), demonstrates a comparatively lower signal attenuation of 39.2 % after photobleaching, whereas 4-nitrophenol exhibits a signal decrease of 68.1 %. The electron-withdrawing substituents exert both inductive and resonance effects, effectively diminishing the electron density of the π-system of the aromatic ring. This electron-deficient state enhances the susceptibility of these species to nucleophilic attack by OH radicals, thereby facilitating their photooxidation and contributing to the observed photobleaching behavior. However, the reactivity of these species remains lower than that of MG and 2-IC oligomers, which explains lower k_{BrC} for p-BrC compares to aq-BrC.

In comparison, the signal intensities of the majority of lignin derivatives only decreased by below 50 %, corresponding to the lowest k_{BrC} for b-BrC (Fig. 3c). Specifically, nodakenetin and flavonoids (m/z 245.08, 283.06,

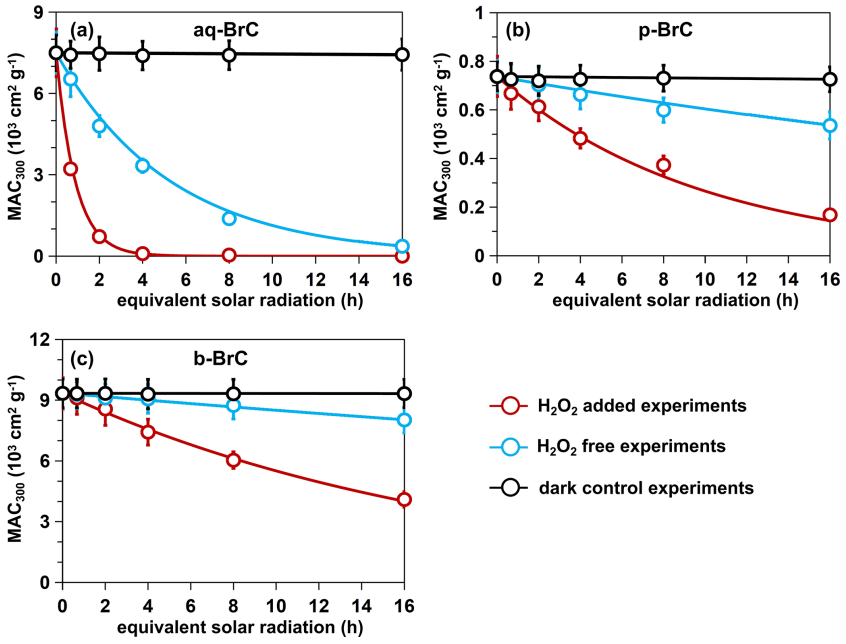

Figure 2. The variations in MAC_{300} in photochemical aging experiments (with H_2O_2, red line, representing the synergistic effect of OH oxidation, direct BrC photolysis, and other light-independent reactions occur in dark conditions), H_2O_2 free experiments (blue line, representing the variation in MAC_{300} contributed by BrC direct photolysis), and dark control experiments (black line, representing the variation in MAC_{300} contributed by other light-independent reactions occur in dark conditions) for **(a)** aq-BrC, **(b)** p-BrC, and **(c)** b-BrC, respectively. For dark control experiments (black line), the x axis represents the time the BrC solution is kept in the absence of light.

Table 2. Variations in the signal-intensity-weighted average elemental compositions, molecular weights, O/C ratios, and N/C ratios of different types of BrC before and after photobleaching.

aq-BrC	elemental composition	molecular weight	O/C	N/C
before	$C_{8.94}H_{10.22}O_{4.64}N_{1.33}$	210.36	0.52	0.15
after	$C_{8.22}H_{10.17}O_{4.66}N_{1.07}$	198.35	0.57	0.12
p-BrC	elemental composition	molecular weight	O/C	N/C
before	$C_{7.88}H_{8.38}O_{2.47}N_{2.13}S_{0.65}$	193.08	0.31	0.28
after	$C_{7.21}H_{9.17}O_{2.52}N_{1.82}S_{0.68}$	183.25	0.35	0.25
b-BrC	elemental composition	molecular weight	O/C	N/C
before	$C_{15.92}H_{16.68}O_{6.05}N_{1.18}S_{0.31}$	330.96	0.38	0.08
after	$C_{15.42}H_{16.92}O_{6.11}N_{1.07}S_{0.41}$	327.82	0.40	0.07

and 313.07) exhibit highly stabilized molecular structures, wherein the aromatic rings conjugated with oxygen-containing heterocyclic moieties significantly reduce their chemical reactivity, resulting in low k_{BrC} for b-BrC. The chemical stability of lignin derivatives has been also proved by previous laboratory experiment (Wong et al., 2019). However, studies found that levoglucosan, which is an important component in biomass burning aerosols, may be oxidized by OH radicals and therefore slow down the reaction of other BrC chromophores reacting with OH (Bai et al., 2013; Zhao et al., 2014). In this work, the same TOC mass concentrations (50 mg L^{-1}) across all BrC types provides equal total potential OH sinks, making the observed order-of-magnitude difference in k_{BrC} more likely attributable to the reactivity of the chromophores themselves rather than solely to differences in competitor abundance. Additionally, the identified lignin derivatives exhibited low signal decay percentages despite being exposed to the same $[OH]_{ss}$ as the highly reactive BrC chromophores. Hence, it is expected that the chemical stability of lignin derivative leads to the low k_{BrC} for b-BrC.

We noted that the exact variation in the mass concentration of compounds shown in Fig. 3 were not derived in this work. Ultra-high performance liquid chromatography (UHPLC)-HRMS analysis using standards or surrogate stan-

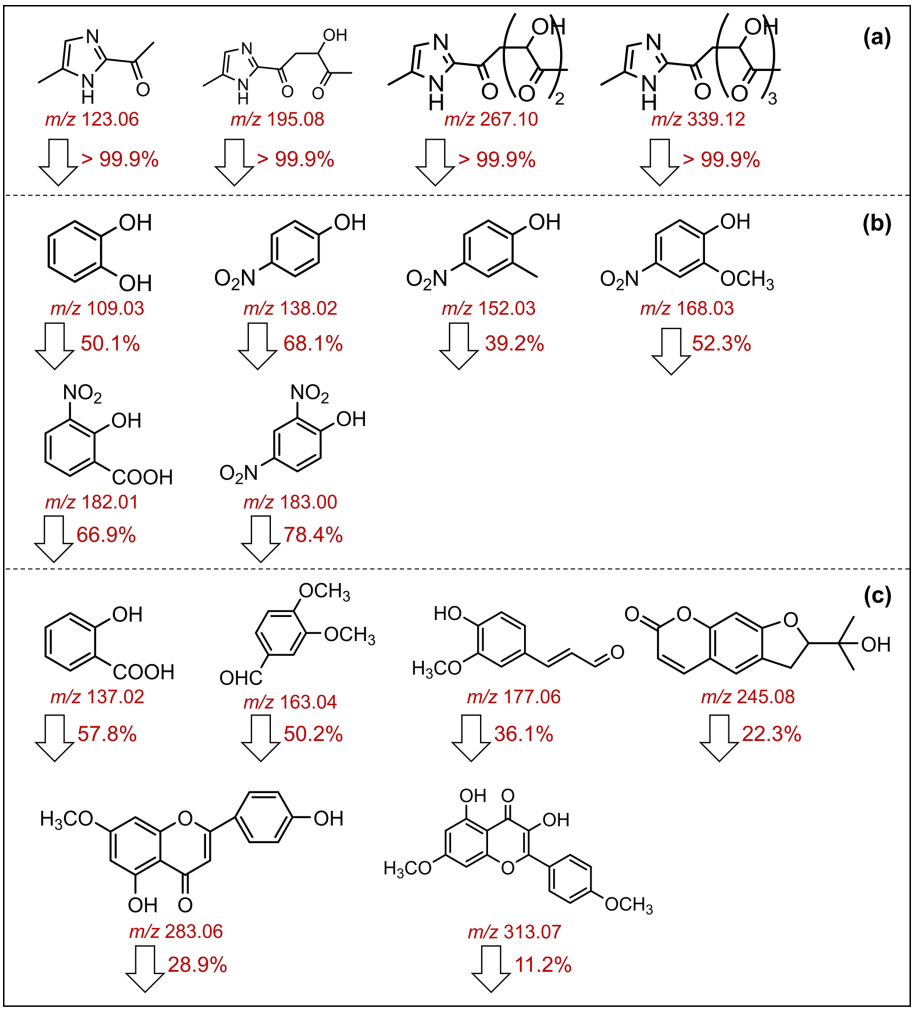

Figure 3. The chemical structures of **(a)** MG and 2-IC oligomers detected in aq-BrC; **(b)** phenols and nitrophenols detected in p-BrC, and **(c)** lignin derivatives detected in b-BrC. The detected m/z for these compounds are marked under their structures. The ratios of decline in signal intensities for these compounds after 16 h of radiation are indicated next to the bottom arrows.

dards should be adopted to obtain the mass concentration of these compounds. However, this work aims to comparatively track the changes in molecular composition for each specific BrC type before and after photobleaching. While absolute quantification is not feasible based on HRMS analysis, the relative changes in signal intensity for a given compound are comparable within the same sample matrix. Therefore, the variation in signal intensity for a specific m/z can be reliably interpreted as a corresponding change in its relative mass concentration.

In addition, while the species highlighted in Fig. 3 were rigorously selected as representative and reactive chromophores through the differential screening and structural identification process described above, we fully acknowledge that our analysis may not capture all potential BrC chromophores. Limitations in analytical sensitivity, chromatographic separation, and the chemical complexity of BrC result in several BrC chromophores, particularly those at low concentrations or with poor ionization efficiency, might not be detected or their changes fully characterized. Therefore, while the reported decay percentages for the identified species are robust, the total BrC photobleaching likely involves contributions from additional chromophores not specifically tracked here.

4 Conclusion and Atmospheric Implication

This work quantifies the k_{BrC} for three different types of BrC and demonstrates that their order-of-magnitude differences (aq-BrC > p-BrC > b-BrC) originate from distinct molecular susceptibilities to OH-driven oxidation through controlled comparative experiments. While the source dependency of BrC photobleaching has been suggested, our study mechanistically establishes the linkage between BrC photobleach-

ing kinetics and molecular composition. Specifically, rapid photobleaching of aq-BrC is governed by the high OH reactivity of MG and 2-IC oligomers; in comparison, the remarkable stability of b-BrC is attributed to resilient, conjugated aromatic systems in lignin derivatives. For p-BrC, an intermediate k_{BrC} was observed, consistent with the oxidation kinetics of nitrophenolic chromophores. Critically, we show that OH oxidation accounts for $> 80\,\%$ of the total photobleaching across all sources, identifying it as the dominant and unifying chemical pathway under aqueous conditions.

These quantified, source-dependent k_{BrC} values and their molecular-level changes emphasizes the necessitate explicit consideration of source variability when evaluating BrC's radiative effect. Current models often assume constant k_{BrC} based on simplified representative compounds or field data (Hems and Abbatt, 2018; Schnitzler et al., 2022; Wang et al., 2018), yet substantial discrepancies exist. For instance, the reported k_{BrC} values differ by approximately an order of magnitude between field observations and laboratory simulations (Schnitzler et al., 2022; Wang et al., 2018). Spatiotemporal heterogeneity in BrC sources (Xiong et al., 2022) (fossil fuel/biomass combustion, secondary formation) drives global regional variations in k_{BrC}. We should acknowledge that though source-dependent BrC photobleaching rates are essential in assessing BrC's global DRE, the impact of environmental conditions like temperature and relative humidity are also decisive (Schnitzler et al., 2022).

In addition, the low k_{BrC} for b-BrC explains unexpectedly high BrC absorption in remote regions (e.g., the Arctic). Field data confirm biomass burning contributes 57 % of Arctic BrC while $< 10\,\%$ for secondary BrC (Yue et al., 2022). Previous studies have confirmed that biomass burning aerosols contains substantial amounts of lignin derivatives (Wong et al., 2019), which exhibit strong light-absorbing properties and chemical stability in OH oxidation. Therefore, during the long-range transport (Zhang et al., 2025), b-BrC is expected to retain strong absorption, leading to enhancement of the aerosol DRE over large spatial scales. On a global scale, one major source of b-BrC is wildfire events (Wang et al., 2025; Shen et al., 2024; Bond et al., 2004). With the increasing frequency of wildfires (Yue et al., 2013; Hurteau et al., 2014; Cunningham et al., 2024; Jain et al., 2022), the emission of b-BrC is expected to rise correspondingly. In all, b-BrC would exert a significant influence on BrC's global radiative effect.

Data availability. The data used in this study is available upon request from the corresponding author (zhijunwu@pku.edu.cn).

Supplement. The supplement related to this article is available online at https://doi.org/10.5194/acp-26-2785-2026-supplement.

Author contributions. Y.Q. and Z.W. designed this work. Y.Q., T.Q., Y.G., and D.L. collected and analyzed the measurement data. Y.Q., T.Q., Y.L, and R.M. analyzed HRMS data. Z.W. and M.H. edited the manuscript. All authors have read and agreed to submit this manuscript.

Competing interests. The contact author has declared that none of the authors has any competing interests.

Disclaimer. Publisher's note: Copernicus Publications remains neutral with regard to jurisdictional claims made in the text, published maps, institutional affiliations, or any other geographical representation in this paper. The authors bear the ultimate responsibility for providing appropriate place names. Views expressed in the text are those of the authors and do not necessarily reflect the views of the publisher.

Financial support. This work is funded by National Natural Science Foundation of China – Youth Program (grant no. 42507137), China Postdoctoral Science Foundation (grant no. 2025M771267), and the National Key Research and Development Program of China (grant no. 2022YFC3701000, Task 4).

Review statement. This paper was edited by Sergey A. Nizkorodov and reviewed by two anonymous referees.

References

Aiona, P. K., Lee, H. J., Leslie, R., Lin, P., Laskin, A., Laskin, J., and Nizkorodov, S. A.: Photochemistry of Products of the Aqueous Reaction of Methylglyoxal with Ammonium Sulfate, ACS Earth and Space Chemistry, 1, 522–532, https://doi.org/10.1021/acsearthspacechem.7b00075, 2017.

Bai, J., Sun, X., Zhang, C., Xu, Y., and Qi, C.: The OH-initiated atmospheric reaction mechanism and kinetics for levoglucosan emitted in biomass burning, Chemosphere, 93, 2004–2010, https://doi.org/10.1016/j.chemosphere.2013.07.021, 2013.

Bond, T. C.: Spectral dependence of visible light absorption by carbonaceous particles emitted from coal combustion, Geophysical Research Letters, 28, 4075–4078, https://doi.org/10.1029/2001GL013652, 2001.

Bond, T. C., Streets, D. G., Yarber, K. F., Nelson, S. M., Woo, J.-H., and Klimont, Z.: A technology-based global inventory of black and organic carbon emissions from combustion, Journal of Geophysical Research: Atmospheres, 109, https://doi.org/10.1029/2003JD003697, 2004.

Borduas-Dedekind, N., Ossola, R., David, R. O., Boynton, L. S., Weichlinger, V., Kanji, Z. A., and McNeill, K.: Photomineralization mechanism changes the ability of dissolved organic matter to activate cloud droplets and to nucleate ice crystals, Atmos. Chem. Phys., 19, 12397–12412, https://doi.org/10.5194/acp-19-12397-2019, 2019.

Brown, H., Liu, X., Pokhrel, R., Murphy, S., Lu, Z., Saleh, R., Mielonen, T., Kokkola, H., Bergman, T., Myhre, G., Skeie,

R. B., Watson-Paris, D., Stier, P., Johnson, B., Bellouin, N., Schulz, M., Vakkari, V., Beukes, J. P., van Zyl, P. G., Liu, S., and Chand, D.: Biomass burning aerosols in most climate models are too absorbing, Nature Communications, 12, 277, https://doi.org/10.1038/s41467-020-20482-9, 2021.

Chen, L.-W. A., Chow, J. C., Wang, X., Cao, J., Mao, J., and Watson, J. G.: Brownness of Organic Aerosol over the United States: Evidence for Seasonal Biomass Burning and Photobleaching Effects, Environmental Science & Technology, 55, 8561–8572, https://doi.org/10.1021/acs.est.0c08706, 2021.

Chen, Q., Sun, H., Wang, J., Shan, M., Yang, X., Deng, M., Wang, Y., and Zhang, L.: Long-life type – The dominant fraction of EPFRs in combustion sources and ambient fine particles in Xi'an, Atmos. Environ., 219, 117059, https://doi.org/10.1016/j.atmosenv.2019.117059, 2019.

Choudhary, V., Roson, M. L., Guo, X., Gautam, T., Gupta, T., and Zhao, R.: Aqueous-phase photochemical oxidation of water-soluble brown carbon aerosols arising from solid biomass fuel burning, Environmental Science: Atmospheres, 3, 816–829, https://doi.org/10.1039/D2EA00151A, 2023.

Chung, C. E., Ramanathan, V., and Decremer, D.: Observationally constrained estimates of carbonaceous aerosol radiative forcing, Proceedings of the National Academy of Sciences USA, 109, 11624–11629, https://doi.org/10.1073/pnas.1203707109, 2012.

Corr, C. A., Hall, S. R., Ullmann, K., Anderson, B. E., Beyersdorf, A. J., Thornhill, K. L., Cubison, M. J., Jimenez, J. L., Wisthaler, A., and Dibb, J. E.: Spectral absorption of biomass burning aerosol determined from retrieved single scattering albedo during ARCTAS, Atmos. Chem. Phys., 12, 10505–10518, https://doi.org/10.5194/acp-12-10505-2012, 2012.

Cunningham, C. X., Williamson, G. J., and Bowman, D. M. J. S.: Increasing frequency and intensity of the most extreme wildfires on Earth, Nature Ecology & Evolution, 8, 1420–1425, https://doi.org/10.1038/s41559-024-02452-2, 2024.

Dalton, A. B. and Nizkorodov, S. A.: Photochemical Degradation of 4-Nitrocatechol and 2,4-Dinitrophenol in a Sugar-Glass Secondary Organic Aerosol Surrogate, Environmental Science & Technology, 55, 14586–14594, https://doi.org/10.1021/acs.est.1c04975, 2021.

Dasari, S., Andersson, A., Bikkina, S., Holmstrand, H., Budhavant, K., Satheesh, S., Asmi, E., Kesti, J., Backman, J., Salam, A., Bisht, D. S., Tiwari, S., Hameed, Z., and Gustafsson, Ö.: Photochemical degradation affects the light absorption of water-soluble brown carbon in the South Asian outflow, Science Advances, 5, eaau8066, https://doi.org/10.1126/sciadv.aau8066, 2019.

De Haan, D. O., Hawkins, L. N., Welsh, H. G., Pednekar, R., Casar, J. R., Pennington, E. A., de Loera, A., Jimenez, N. G., Symons, M. A., Zauscher, M., Pajunoja, A., Caponi, L., Cazaunau, M., Formenti, P., Gratien, A., Pangui, E., and Doussin, J.-F.: Brown Carbon Production in Ammonium- or Amine-Containing Aerosol Particles by Reactive Uptake of Methylglyoxal and Photolytic Cloud Cycling, Environmental Science & Technology, 51, 7458–7466, https://doi.org/10.1021/acs.est.7b00159, 2017.

Fan, X., Yu, X., Wang, Y., Xiao, X., Li, F., Xie, Y., Wei, S., Song, J., and Peng'an, P.: The aging behaviors of chromophoric biomass burning brown carbon during dark aqueous hydroxyl radical oxidation processes in laboratory studies, Atmospheric Environment, 205, 9–18, https://doi.org/10.1016/j.atmosenv.2019.02.039, 2019.

Fleming, L. T., Ali, N. N., Blair, S. L., Roveretto, M., George, C., and Nizkorodov, S. A.: Formation of Light-Absorbing Organosulfates during Evaporation of Secondary Organic Material Extracts in the Presence of Sulfuric Acid, ACS Earth and Space Chemistry, 3, 947–957, https://doi.org/10.1021/acsearthspacechem.9b00036, 2019.

Fleming, L. T., Lin, P., Roberts, J. M., Selimovic, V., Yokelson, R., Laskin, J., Laskin, A., and Nizkorodov, S. A.: Molecular composition and photochemical lifetimes of brown carbon chromophores in biomass burning organic aerosol, Atmos. Chem. Phys., 20, 1105–1129, https://doi.org/10.5194/acp-20-1105-2020, 2020.

Fu, T.-M., Jacob, D. J., Wittrock, F., Burrows, J. P., Vrekoussis, M., and Henze, D. K.: Global budgets of atmospheric glyoxal and methylglyoxal, and implications for formation of secondary organic aerosols, Journal of Geophysical Research: Atmospheres, 113, https://doi.org/10.1029/2007JD009505, 2008.

Gao, Y. and Zhang, Y.: Optical properties investigation of the reactions between methylglyoxal and glycine/ammonium sulfate, Spectrochimica Acta Part A: Molecular and Biomolecular Spectroscopy, 215, 112–121, https://doi.org/10.1016/j.saa.2019.02.087, 2019.

Gu, J., Dutta, S., Sioud, S., Go, B. R., Maity, B., Cavallo, L., Zhang, R., and Chan, C. K.: Photoinduced Transformation in Glyoxal- and Methylglyoxal-Ammonium Solutions: Role of Photolysis and Photosensitization, Environmental Science & Technology, 59, 16628–16640, https://doi.org/10.1021/acs.est.5c04889, 2025.

Heald, C. L., Ridley, D. A., Kroll, J. H., Barrett, S. R. H., Cady-Pereira, K. E., Alvarado, M. J., and Holmes, C. D.: Contrasting the direct radiative effect and direct radiative forcing of aerosols, Atmos. Chem. Phys., 14, 5513–5527, https://doi.org/10.5194/acp-14-5513-2014, 2014.

Hems, R. F. and Abbatt, J. P. D.: Aqueous Phase Photooxidation of Brown Carbon Nitrophenols: Reaction Kinetics, Mechanism, and Evolution of Light Absorption, ACS Earth and Space Chemistry, 2, 225–234, https://doi.org/10.1021/acsearthspacechem.7b00123, 2018.

Hems, R. F., Schnitzler, E. G., Bastawrous, M., Soong, R., Simpson, A. J., and Abbatt, J. P. D.: Aqueous Photoreactions of Wood Smoke Brown Carbon, ACS Earth and Space Chemistry, 4, 1149–1160, https://doi.org/10.1021/acsearthspacechem.0c00117, 2020.

Hems, R. F., Schnitzler, E. G., Liu-Kang, C., Cappa, C. D., and Abbatt, J. P. D.: Aging of Atmospheric Brown Carbon Aerosol, ACS Earth and Space Chemistry, 5, 722–748, https://doi.org/10.1021/acsearthspacechem.0c00346, 2021.

Hurteau, M. D., Westerling, A. L., Wiedinmyer, C., and Bryant, B. P.: Projected Effects of Climate and Development on California Wildfire Emissions through 2100, Environmental Science & Technology, 48, 2298–2304, https://doi.org/10.1021/es4050133, 2014.

Jain, P., Castellanos-Acuna, D., Coogan, S. C. P., Abatzoglou, J. T., and Flannigan, M. D.: Observed increases in extreme fire weather driven by atmospheric humidity and temperature, Nature Climate Change, 12, 63–70, https://doi.org/10.1038/s41558-021-01224-1, 2022.

Jo, D. S., Park, R. J., Lee, S., Kim, S.-W., and Zhang, X.: A global simulation of brown carbon: implications for photochemistry and direct radiative effect, Atmos. Chem. Phys., 16, 3413–3432, https://doi.org/10.5194/acp-16-3413-2016, 2016.

Kirchstetter, T. W., Novakov, T., and Hobbs, P. V.: Evidence that the spectral dependence of light absorption by aerosols is affected by organic carbon, Journal of Geophysical Research: Atmospheres, 109, https://doi.org/10.1029/2004JD004999, 2004.

Laskin, A., Laskin, J., and Nizkorodov, S. A.: Chemistry of Atmospheric Brown Carbon, Chemical Reviews, 115, 4335–4382, https://doi.org/10.1021/cr5006167, 2015.

Li, Y., Fu, T.-M., Yu, J. Z., Zhang, A., Yu, X., Ye, J., Zhu, L., Shen, H., Wang, C., Yang, X., Tao, S., Chen, Q., Li, Y., Li, L., Che, H., and Heald, C. L.: Nitrogen dominates global atmospheric organic aerosol absorption, Science, 387, 989–995, https://doi.org/10.1126/science.adr4473, 2025.

Lin, P., Huang, X.-F., He, L.-Y., and Zhen Yu, J.: Abundance and size distribution of HULIS in ambient aerosols at a rural site in South China, Journal of Aerosol Science, 41, 74–87, https://doi.org/10.1016/j.jaerosci.2009.09.001, 2010.

Lin, P., Bluvshtein, N., Rudich, Y., Nizkorodov, S. A., Laskin, J., and Laskin, A.: Molecular Chemistry of Atmospheric Brown Carbon Inferred from a Nationwide Biomass Burning Event, Environmental Science & Technology, 51, 11561–11570, https://doi.org/10.1021/acs.est.7b02276, 2017.

Liu-Kang, C., Gallimore, P. J., Liu, T., and Abbatt, J. P. D.: Photoreaction of biomass burning brown carbon aerosol particles, Environmental Science: Atmospheres, 2, 270–278, https://doi.org/10.1039/d1ea00088h, 2022.

Liu, D., He, C., Schwarz, J. P., and Wang, X.: Lifecycle of light-absorbing carbonaceous aerosols in the atmosphere, npj Climate and Atmospheric Science, 3, 40, https://doi.org/10.1038/s41612-020-00145-8, 2020.

Liu, Y., Huang, R.-J., Lin, C., Yuan, W., Li, Y. J., Zhong, H., Yang, L., Wang, T., Huang, W., Xu, W., Huang, D. D., and Huang, C.: Nitrate-Photolysis Shortens the Lifetimes of Brown Carbon Tracers from Biomass Burning, Environmental Science & Technology, 59, 640–649, https://doi.org/10.1021/acs.est.4c06123, 2025.

Magalhães, A. C. O., Esteves da Silva, J. C. G., and Pinto da Silva, L.: Density Functional Theory Calculation of the Absorption Properties of Brown Carbon Chromophores Generated by Catechol Heterogeneous Ozonolysis, ACS Earth and Space Chemistry, 1, 353–360, https://doi.org/10.1021/acsearthspacechem.7b00061, 2017.

Müller, S., Giorio, C., and Borduas-Dedekind, N.: Tracking the Photomineralization Mechanism in Irradiated Lab-Generated and Field-Collected Brown Carbon Samples and Its Effect on Cloud Condensation Nuclei Abilities, ACS Environmental Au, 3, 164–178, https://doi.org/10.1021/acsenvironau.2c00055, 2023.

Qiu, Y., Qiu, T., Wu, Z., Liu, Y., Fang, W., Man, R., Liu, Y., Wang, J., Meng, X., Chen, J., Liang, D., Guo, S., and Hu, M.: Observational Evidence of Brown Carbon Photobleaching in Urban Atmosphere at Molecular Level, Environmental Science and Technology Letters, 11, 1032–1039, https://doi.org/10.1021/acs.estlett.4c00647, 2024.

Saleh, R.: From Measurements to Models: Toward Accurate Representation of Brown Carbon in Climate Calculations, Current Pollution Reports, 6, 90–104, https://doi.org/10.1007/s40726-020-00139-3, 2020.

Saleh, R., Marks, M., Heo, J., Adams, P. J., Donahue, N. M., and Robinson, A. L.: Contribution of brown carbon and lensing to the direct radiative effect of carbonaceous aerosols from biomass and biofuel burning emissions, Journal of Geophysical Research: Atmospheres, 120, 10285–10296, https://doi.org/10.1002/2015JD023697, 2015.

Schnitzler, E. G. and Abbatt, J. P. D.: Heterogeneous OH oxidation of secondary brown carbon aerosol, Atmos. Chem. Phys., 18, 14539–14553, https://doi.org/10.5194/acp-18-14539-2018, 2018.

Schnitzler, E. G., Gerrebos, N. G. A., Carter, T. S., Huang, Y., Heald, C. L., Bertram, A. K., and Abbatt, J. P. D.: Rate of atmospheric brown carbon whitening governed by environmental conditions, Proceedings of the National Academy of Sciences, 119, e2205610119, https://doi.org/10.1073/pnas.2205610119, 2022.

Shan, M., Carter, E., Baumgartner, J., Deng, M., Clark, S., Schauer, J. J., Ezzati, M., Li, J., Fu, Y., and Yang, X.: A user-centered, iterative engineering approach for advanced biomass cookstove design and development, Environ. Res. Lett., 12, 095009, https://doi.org/10.1088/1748-9326/aa804f, 2017.

Shen, Y., Pokhrel, R. P., Sullivan, A. P., Levin, E. J. T., Garofalo, L. A., Farmer, D. K., Permar, W., Hu, L., Toohey, D. W., Campos, T., Fischer, E. V., and Murphy, S. M.: Understanding the mechanism and importance of brown carbon bleaching across the visible spectrum in biomass burning plumes from the WE-CAN campaign, Atmos. Chem. Phys., 24, 12881–12901, https://doi.org/10.5194/acp-24-12881-2024, 2024.

Wang, Q., Zhou, Y., Ma, N., Zhu, Y., Zhao, X., Zhu, S., Tao, J., Hong, J., Wu, W., Cheng, Y., and Su, H.: Review of Brown Carbon Aerosols in China: Pollution Level, Optical Properties, and Emissions, Journal of Geophysical Research: Atmospheres, 127, e2021JD035473, https://doi.org/10.1029/2021JD035473, 2022.

Wang, X., Heald, C. L., Ridley, D. A., Schwarz, J. P., Spackman, J. R., Perring, A. E., Coe, H., Liu, D., and Clarke, A. D.: Exploiting simultaneous observational constraints on mass and absorption to estimate the global direct radiative forcing of black carbon and brown carbon, Atmos. Chem. Phys., 14, 10989–11010, https://doi.org/10.5194/acp-14-10989-2014, 2014.

Wang, X., Heald, C. L., Liu, J., Weber, R. J., Campuzano-Jost, P., Jimenez, J. L., Schwarz, J. P., and Perring, A. E.: Exploring the observational constraints on the simulation of brown carbon, Atmos. Chem. Phys., 18, 635–653, https://doi.org/10.5194/acp-18-635-2018, 2018.

Wang, X., Chakrabarty, R. K., Schwarz, J. P., Murphy, S. M., Levin, E. J. T., Howell, S. G., Guo, H., Campuzano-Jost, P., and Jimenez, J. L.: Dark brown carbon from biomass burning contributes to significant global-scale positive forcing, One Earth, 8, 101205, https://doi.org/10.1016/j.oneear.2025.101205, 2025.

Wang, Y., Hu, M., Lin, P., Guo, Q., Wu, Z., Li, M., Zeng, L., Song, Y., Zeng, L., Wu, Y., Guo, S., Huang, X., and He, L.: Molecular Characterization of Nitrogen-Containing Organic Compounds in Humic-like Substances Emitted from Straw Residue Burning, Environmental Science & Technology, 51, 5951–5961, https://doi.org/10.1021/acs.est.7b00248, 2017.

Wang, Y., Hu, M., Lin, P., Tan, T., Li, M., Xu, N., Zheng, J., Du, Z., Qin, Y., Wu, Y., Lu, S., Song, Y., Wu, Z., Guo, S., Zeng, L., Huang, X., and He, L.: Enhancement in Particulate Organic Ni-

trogen and Light Absorption of Humic-Like Substances over Tibetan Plateau Due to Long-Range Transported Biomass Burning Emissions, Environmental Science & Technology, 53, 14222–14232, https://doi.org/10.1021/acs.est.9b06152, 2019.

Wong, J. P. S., Tsagkaraki, M., Tsiodra, I., Mihalopoulos, N., Violaki, K., Kanakidou, M., Sciare, J., Nenes, A., and Weber, R. J.: Atmospheric evolution of molecular-weight-separated brown carbon from biomass burning, Atmos. Chem. Phys., 19, 7319–7334, https://doi.org/10.5194/acp-19-7319-2019, 2019.

Xiong, R., Li, J., Zhang, Y., Zhang, L., Jiang, K., Zheng, H., Kong, S., Shen, H., Cheng, H., Shen, G., and Tao, S.: Global brown carbon emissions from combustion sources, Environmental Science and Ecotechnology, 12, 100201, https://doi.org/10.1016/j.ese.2022.100201, 2022.

Xu, L., Lin, G., Liu, X., Wu, C., Wu, Y., and Lou, S.: Constraining Light Absorption of Brown Carbon in China and Implications for Aerosol Direct Radiative Effect, Geophysical Research Letters, 51, e2024GL109861, https://doi.org/10.1029/2024GL109861, 2024.

Yang, L., Huang, R.-J., Yuan, W., Huang, D. D., and Huang, C.: pH-Dependent Aqueous-Phase Brown Carbon Formation: Rate Constants and Implications for Solar Absorption and Atmospheric Photochemistry, Environmental Science & Technology, 1236–1243, https://doi.org/10.1021/acs.est.3c07631, 2024.

Yue, S., Zhu, J., Chen, S., Xie, Q., Li, W., Li, L., Ren, H., Su, S., Li, P., Ma, H., Fan, Y., Cheng, B., Wu, L., Deng, J., Hu, W., Ren, L., Wei, L., Zhao, W., Tian, Y., Pan, X., Sun, Y., Wang, Z., Wu, F., Liu, C.-Q., Su, H., Penner, J. E., Pöschl, U., Andreae, M. O., Cheng, Y., and Fu, P.: Brown carbon from biomass burning imposes strong circum-Arctic warming, One Earth, 5, 293–304, https://doi.org/10.1016/j.oneear.2022.02.006, 2022.

Yue, X., Mickley, L. J., Logan, J. A., and Kaplan, J. O.: Ensemble projections of wildfire activity and carbonaceous aerosol concentrations over the western United States in the mid-21st century, Atmospheric Environment, 77, 767–780, https://doi.org/10.1016/j.atmosenv.2013.06.003, 2013.

Zeng, L., Zhang, A., Wang, Y., Wagner, N. L., Katich, J. M., Schwarz, J. P., Schill, G. P., Brock, C., Froyd, K. D., Murphy, D. M., Williamson, C. J., Kupc, A., Scheuer, E., Dibb, J., and Weber, R. J.: Global Measurements of Brown Carbon and Estimated Direct Radiative Effects, Geophysical Research Letters, 47, e2020GL088747, https://doi.org/10.1029/2020GL088747, 2020.

Zeng, Y., Ning, Y., Shen, Z., Zhang, L., Zhang, T., Lei, Y., Zhang, Q., Li, G., Xu, H., Ho, S. S. H., and Cao, J.: The Roles of N, S, and O in Molecular Absorption Features of Brown Carbon in PM2.5 in a Typical Semi-Arid Megacity in Northwestern China, Journal of Geophysical Research: Atmospheres, 126, e2021JD034791, https://doi.org/10.1029/2021JD034791, 2021.

Zhang, Q., Wang, Y., Xiao, Q., Geng, G., Davis, S. J., Liu, X., Yang, J., Liu, J., Huang, W., He, C., Luo, B., Martin, R. V., Brauer, M., Randerson, J. T., and He, K.: Long-range PM2.5 pollution and health impacts from the 2023 Canadian wildfires, Nature, https://doi.org/10.1038/s41586-025-09482-1, 2025.

Zhang, X., Chen, S., Kang, L., Yuan, T., Luo, Y., Alam, K., Li, J., He, Y., Bi, H., and Zhao, D.: Direct Radiative Forcing Induced by Light-Absorbing Aerosols in Different Climate Regions Over East Asia, Journal of Geophysical Research: Atmospheres, 125, e2019JD032228, https://doi.org/10.1029/2019JD032228, 2020.

Zhao, R., Mungall, E. L., Lee, A. K. Y., Aljawhary, D., and Abbatt, J. P. D.: Aqueous-phase photooxidation of levoglucosan – a mechanistic study using aerosol time-of-flight chemical ionization mass spectrometry (Aerosol ToF-CIMS), Atmos. Chem. Phys., 14, 9695–9706, https://doi.org/10.5194/acp-14-9695-2014, 2014.

Zhao, R., Lee, A. K. Y., Huang, L., Li, X., Yang, F., and Abbatt, J. P. D.: Photochemical processing of aqueous atmospheric brown carbon, Atmos. Chem. Phys., 15, 6087–6100, https://doi.org/10.5194/acp-15-6087-2015, 2015.